



**CHALMERS**  
UNIVERSITY OF TECHNOLOGY

## Unusually large magnetic moment and tricritical behavior of the CMR compound $\text{NaCr}_2\text{O}_4$ revealed with high resolution

Downloaded from: <https://research.chalmers.se>, 2024-05-06 00:18 UTC

Citation for the original published paper (version of record):

Nocerino, E., Forslund, O., Sakurai, H. et al (2023). Unusually large magnetic moment and tricritical behavior of the CMR compound

$\text{NaCr}_2\text{O}_4$  revealed with high resolution neutron diffraction and  $\mu + \text{SR}$ . JPhys Materials, 6(3). <http://dx.doi.org/10.1088/2515-7639/acdf21>

N.B. When citing this work, cite the original published paper.

PAPER • OPEN ACCESS

## Unusually large magnetic moment and tricritical behavior of the CMR compound $\text{NaCr}_2\text{O}_4$ revealed with high resolution neutron diffraction and $\mu^+$ SR

To cite this article: Elisabetta Nocerino *et al* 2023 *J. Phys. Mater.* **6** 035009

View the [article online](#) for updates and enhancements.

### You may also like

- [Magnetic couplings in edge-sharing high-spin  \$d^7\$  compounds](#)  
Stephen M Winter
- [Charge transfer state characterization and voltage losses of organic solar cells](#)  
Anna Jungbluth, Pascal Kaienburg and Moritz Riede
- [Protocol for generating an arbitrary quantum state of the magnetization in cavity magnonics](#)  
Sanchar Sharma, Victor A S V Bittencourt and Silvia Viola Kusminskiy



### 244th ECS Meeting

Gothenburg, Sweden • Oct 8 – 12, 2023

Early registration pricing ends  
September 11

Register and join us in advancing science!



[Learn More & Register Now!](#)



## OPEN ACCESS

RECEIVED  
9 March 2023REVISED  
4 May 2023ACCEPTED FOR PUBLICATION  
16 June 2023PUBLISHED  
4 July 2023

Original Content from  
this work may be used  
under the terms of the  
[Creative Commons  
Attribution 4.0 licence](#).

Any further distribution  
of this work must  
maintain attribution to  
the author(s) and the title  
of the work, journal  
citation and DOI.



## PAPER

Unusually large magnetic moment and tricritical behavior of the CMR compound  $\text{NaCr}_2\text{O}_4$  revealed with high resolution neutron diffraction and  $\mu^+$ SRElisabetta Nocerino<sup>1,\*</sup>, Ola Kenji Forslund<sup>2</sup>, Hiroya Sakurai<sup>3</sup>, Akinori Hoshikawa<sup>4</sup>, Nami Matsubara<sup>1</sup>, Daniel Andreica<sup>5</sup>, Anton Zubayer<sup>6</sup>, Federico Mazza<sup>7</sup>, Takashi Saito<sup>8</sup>, Jun Sugiyama<sup>9,10</sup>, Izumi Umegaki<sup>11</sup>, Yasmine Sassa<sup>2</sup> and Martin Månsson<sup>1,\*</sup><sup>1</sup> KTH Royal Institute of Technology, Department of Applied Physics, Alba Nova University Center, Stockholm SE-114 21, Sweden<sup>2</sup> Chalmers University of Technology, Department of Physics, Göteborg SE-412 96, Sweden<sup>3</sup> National Institute for Materials Science, Namiki, Tsukuba, Ibaraki 305-0044, Japan<sup>4</sup> Frontier Research Center for Applied Atomic Sciences, Ibaraki University, 162-1 Shirakata, Tokai, Ibaraki 319-1106, Japan<sup>5</sup> Faculty of Physics, Babes-Bolyai University, 3400 Cluj-Napoca, Romania<sup>6</sup> Department of Physics, Chemistry and Biology (IFM), Linköping University, SE-581 83 Linköping, Sweden<sup>7</sup> Institute of Solid State Physics, TU Wien, Wiedner Hauptstraße 8-10, AT-1040 Wien, Austria<sup>8</sup> Institute of Materials Structure Science, High Energy Accelerator Research Organization, 203-1 Shirakata, Tokai, Ibaraki 319-1107, Japan<sup>9</sup> Neutron Science and Technology Center, Comprehensive Research Organization for Science and Society (CROSS), Tokai, Ibaraki 319-1106, Japan<sup>10</sup> Advanced Science Research Center, Japan Atomic Energy Agency, Tokai, Ibaraki 319-1195, Japan<sup>11</sup> Muon Science Laboratory, Institute of Materials Structure Science, KEK, Tokai, Ibaraki 319-1106, Japan

\* Authors to whom any correspondence should be addressed.

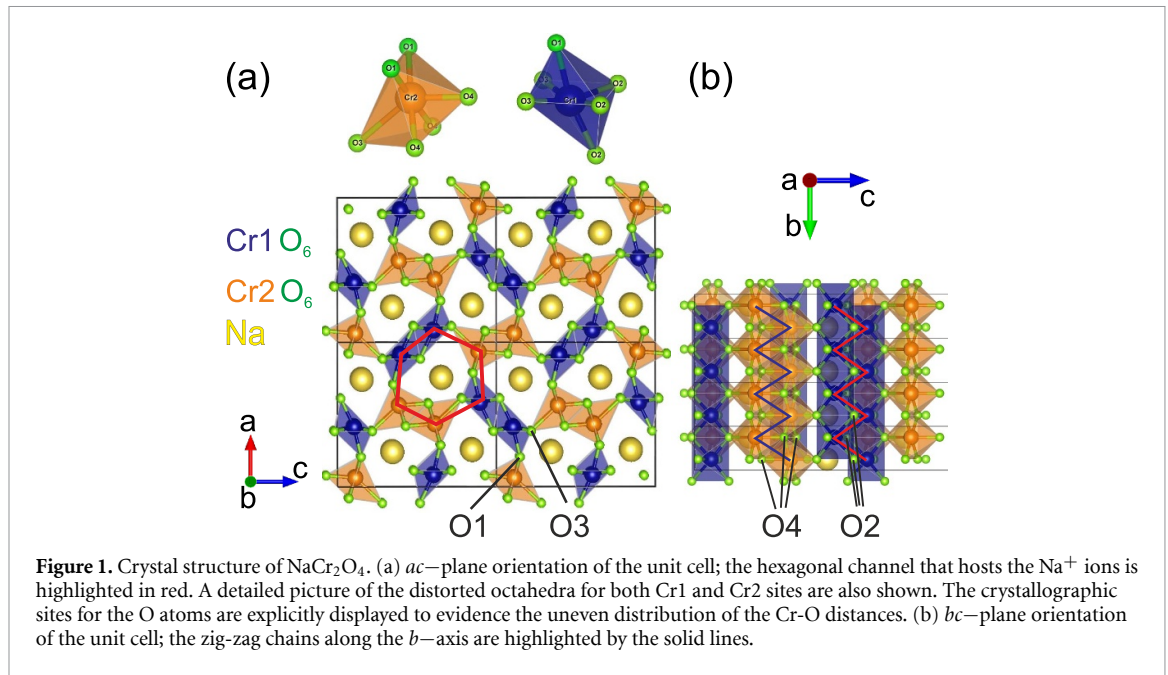
E-mail: [nocerino@kth.se](mailto:nocerino@kth.se) and [condmat@kth.se](mailto:condmat@kth.se)**Keywords:** neutron diffraction, muon spin rotation, unconventional magnetism, colossal magnetoresistance

## Abstract

The mixed valence  $\text{Cr}^{3+}/\text{Cr}^{4+}$  compound  $\text{NaCr}_2\text{O}_4$ , hosts a plethora of unconventional electronic properties. In the present study, muon spin rotation/relaxation ( $\mu^+$ SR) and high-resolution time-of-flight neutron powder diffraction measurements were carried out on high-quality samples to clarify the complex magnetic ground state of this unique material. We identified a commensurate canted antiferromagnetic order (C-AFM) with a canting angle of the Cr spin axial vector equal to  $\theta_c = (8.8 \pm 0.5)^\circ$ , and an estimated Cr moment  $\mu_{\text{Cr}}^{\text{C}} \sim (4.30 \pm 0.01)\mu_{\text{B}}$ . Such an unusually large value of  $\mu_{\text{Cr}}^{\text{C}}$  is compatible with the existence of high-spin Cr sites created by the presence of an unconventional negative charge transfer state in  $\text{NaCr}_2\text{O}_4$ . In addition to the C-AFM structure, a novel magnetic supercell was also revealed. Such supercell display an incommensurate (IC)-AFM propagation vector  $(0\ 0\ \frac{1}{2} - \delta)$ , having a Cr moment  $\mu_{\text{Cr}}^{\text{IC}} = (2.20 \pm 0.03)\mu_{\text{B}}$ . It is suggested that the C-AFM and IC-AFM modulations have two different electronic origins, being due to itinerant and localized contributions to the magnetic moment respectively. Finally, the direct measurement of the magnetic order parameter for the C-AFM structure provided a value of the critical exponent  $\beta = 0.245 \approx \frac{1}{4}$ , suggesting a non conventional critical behavior for the magnetic phase transition in  $\text{NaCr}_2\text{O}_4$ .

## 1. Introduction

Mixed valence transition metal oxides constitute a very attractive scientific playground as they offer a vast range of diverse physical properties, such as unconventional superconductivity, metal–insulator transitions, colossal magneto-resistance (CMR) and exotic magnetic ground states [1–7]. Among them, mixed valence state Cr oxides are rather rare because of the intrinsic stability of  $\text{Cr}^{3+}$  ions in octahedral coordination with O atoms. Here the half-filled  $t_{2g}$  states of the  $3d^3$   $\text{Cr}^{3+}$  orbitals tend to not coexist with  $\text{Cr}^{4+}$  ions, which would instead form a less-than-half filled  $3d^2$  state. Due to the plethora of its unusual physical properties, a lively



interest surrounds the compound  $\text{NaCr}_2\text{O}_4$ . Here, Cr has formal valence  $\text{Cr}^{3.5+}$ , given by the mix in equal parts of  $\text{Cr}^{3+}$  and  $\text{Cr}^{4+}$  valence states [8], which can only be achieved thanks to the high pressure synthesis technique employed to stabilize this material [9]. The high pressure indeed forces a complex crystal-field symmetry and orbital ordering for the Cr ions in  $\text{NaCr}_2\text{O}_4$  [10], which crystallizes in a calcium ferrite-type structure with space group  $Pnma$ . Here, the Cr atoms occupy the two distinct crystallographic positions Cr1 and Cr2, octahedrally coordinated by O atoms (figure 1). The  $\text{CrO}_6$  octahedra associated to the two sites are tilted with respect to the each other and distorted, with  $\text{O}-\widehat{\text{Cr}}-\text{O} \neq 90^\circ$  angles and Cr-O distances that are equal to each other on one side of the octahedron and different of the other side (figure 1(a)), leading to four crystallographically different oxygen sites. The edge sharing connections between the equal Cr-O sides of the octahedra, form zig-zag Cr chains along the  $b$ -axis, via the Cr1-O2-Cr1 and the Cr2-O4-Cr2 bonds. The corner sharing connections between the non-equal Cr-O sides, instead, form rutile slabs in the  $ac$ -plane via the Cr1-O1-Cr2 (along  $a$ ) and the Cr1-O3-Cr2 (along  $c$ ) bonds (figures 1(a) and (b)).

The difference between the two Cr sites lays in their orbital structure, since different distortions in the  $\text{CrO}_6$  octahedra lift the degeneracy on the Cr  $3d$  orbitals in different ways. In particular, following the labelling of the current work, for Cr1 the  $d_{xy}$  orbital is almost fully occupied with a localized nature, while the  $d_{yz\pm xz}$  have an itinerant nature. Vice versa, for Cr2 the  $d_{xy}$  and  $d_{yz+xz}$  are almost fully occupied while the  $d_{yz-xz}$  has an itinerant nature [10]. Such a combination of orbital filling leads to a dual itinerant-localized character for the Cr electrons. Such  $\text{CrO}_6$  network, designs honeycomb-like distorted hexagonal one-dimensional channels (along  $b$ -axis), in which the  $\text{Na}^+$  ions are located (figure 1(a)).

$\text{NaCr}_2\text{O}_4$  exhibits an antiferromagnetic (AFM) transition  $T_N = 125$  K and, below this temperature, it manifests CMR [11] as well. This is already surprising in itself since CMR is usually a physical property related to manganites [12] but, in addition, the CMR of  $\text{NaCr}_2\text{O}_4$  is also anomalous. In conventional CMR systems, the presence of an applied magnetic field causes a dramatic reduction of the electrical resistivity in a limited temperature interval around a ferromagnetic (FM) transition. This effect causes hysteresis in the magnetic and transport measurements, and the system is still metallic even in absence of magnetic field. Under zero magnetic field,  $\text{NaCr}_2\text{O}_4$  behaves as an insulator with its electrical resistivity diverging while cooling. In the presence of an applied magnetic field, the resistivity is dramatically reduced (i.e. the CMR effect), but this effect is not limited to the region of temperatures around the AFM transition. On the contrary, the temperature dependent magnetoresistance curve of  $\text{NaCr}_2\text{O}_4$  increases monotonously, as the temperature decreases, and asymptotically tends to  $-100\%$  for  $T \rightarrow 0$ , without any thermal or field hysteresis [9]. The mechanism underlying conventional CMR in manganites is explained as a magnetic field-induced suppression of the thermal fluctuation of the parallel moments, causing the CMR to disappear at temperatures below the FM transition [13]. Since the CMR in  $\text{NaCr}_2\text{O}_4$  shows a behavior that is the exact opposite of the conventional case, it was concluded that its underlying mechanism must be entirely new.



Beyond the anomalous CMR,  $\text{NaCr}_2\text{O}_4$  was also found to exhibit an unusual coexistence of positive and negative charge transfer states (via XAS measurements [8]). Here, the charge frustration induced by the highly degenerate charge ordering configurations of the  $\text{Cr}^{4+} 3d^2$  electronic state, is removed by establishing a  $3d^3 \bar{\text{L}}$  state (as suggested by  $^{53}\text{Cr}$ -NMR measurements [14]), in which Cr ions share a hole through the ligand oxygen. Calculations of the electronic structure showed that such holes are unevenly distributed and are found preferentially at the corner sharing oxygen sites O1 and O3 [10] (figure 1(a)).

Concerning the magnetic properties of  $\text{NaCr}_2\text{O}_4$ , magnetic susceptibility measurements displayed a large positive value for the Curie-Weiss temperature, indicative of dominant FM interactions. However, the AFM character of the susceptibility (showing the typical AFM cusp), suggested non negligible AFM interactions [9]. Remarkably, a dramatic increase in the magnetization with the application of a relatively small external field of 3.5 T was also observed in bulk magnetic measurements [9]. This behavior was interpreted as a spin-flop transition. Since the Cr zig-zag chains form triangular Cr lattices, it was suggested that a competition between FM and AFM exchange interactions are present within the chains. This would lead to spin frustration (consistent with the supposed spin-flop transition) and a complex magnetic ordering in  $\text{NaCr}_2\text{O}_4$ , similar to the isostructural compounds  $\text{NaV}_2\text{O}_4$  and  $\text{CaCr}_2\text{O}_4$  [7, 15]. The mechanism behind the unconventional CMR in  $\text{NaCr}_2\text{O}_4$  is not understood and is indeed still object of research. However, the fact that it only appears below  $T_N$ , seems to indicate that this effect should be closely related to the magnetic structure. It was suggested that a decrease in the resistivity under the application of an external magnetic field might be attributed to a field-induced enhancement in the mobility of localized Cr electrons [16]. In particular, the field induced re-orientation of the ordered Cr spins would lead to an increase in the hopping probability of the Cr  $d$  electrons, responsible for the magnetic coupling, to preserve their spin angular momentum. The supposed spin frustration in  $\text{NaCr}_2\text{O}_4$  was initially suggested as the main responsible for the presence of the CMR state in this material. Indeed, due to the high degeneracy of the spin state in frustrated systems, the spin structure and consequently the electron hopping probability in  $\text{NaCr}_2\text{O}_4$  would be easily tunable with relatively weak external magnetic fields. An alternative possible explanation for the origin of CMR was suggested to be found in the highly mobile ligand holes introduced by the mixed valence state of Cr ions. Indeed, similarly to the case of Zhang-Rice singlet in cuprates [17], such holes in the  $3d^3 \bar{\text{L}}$  negative charge transfer state of the  $\text{Cr}^{4+}$  ions are strongly correlated with the  $d$ -electrons in the Cr ions, and their mobility would be expected to be dramatically enhanced when the Cr spin is aligned to the external field. These conjectures are at present mainly speculative, further magnetic field-dependent studies of the magnetic spin structure would be needed to clarify the origin of CMR in  $\text{NaCr}_2\text{O}_4$ .

Earlier magnetic measurements of the  $\text{NaCr}_2\text{O}_4$  compound, using muon spin rotation/relaxation ( $\mu^+$ SR) and neutron powder diffraction (NPD) methods, have actually been published [18–20]. Such studies revealed the occurrence of a commensurate canted antiferromagnetic (C-AFM) order with a Néel temperature  $T_N = 125$  K. A spin structure was presented with the Cr moments aligned ferromagnetically along the  $b$ -axis in each chain, and antiferromagnetically in the  $ac$ -plane among adjacent chains, with propagation vector  $k = (1\ 0\ 1)$  [18]. However, the value of the canting angle could not be precisely estimated. In this work we revisit this interesting compound using high-quality samples studied by state-of-the-art  $\mu^+$ SR and high resolution NPD techniques. We present a detailed and thorough study of the temperature dependent magnetic properties in  $\text{NaCr}_2\text{O}_4$  that shed new light on the underlying physics and reveal a series of completely novel properties that were previously overlooked or misinterpreted<sup>12</sup>.

The canting angle of the Cr spin axial vector and its magnitude was clarified in detail. Moreover, an additional incommensurate (IC) modulation of the magnetic structure was observed. A revised mechanism underlying the magnetic ordering was proposed and indications of a tricritical behavior as well as, possibly, metamagnetism emerged from the temperature dependence of the magnetic order parameter. Our results are consistent with the presence of high- and low-spin Cr sites in the magnetic ground state of  $\text{NaCr}_2\text{O}_4$ . Such Cr spin states are also foreseen by a recently published theoretical investigation, according to which a spin disproportionation exists between the Cr1 and Cr2 sites in  $\text{NaCr}_2\text{O}_4$  [22]. The intra-chain FM alignment of the Cr moments along the  $b$ -axis, and a weak coupling between the magnetic ordering and the crystal structure, suggest that no spin frustration is in place along the zigzag chains. In fact, in other Q1D calcium-ferrite type compounds the magnetic order develops along the geometrically frustrated Cr zigzag ladders (e.g.  $\beta$ - $\text{CaCr}_2\text{O}_4$  and  $\text{NaMn}_2\text{O}_4$  [6, 15]). Instead, in  $\text{NaCr}_2\text{O}_4$ , the magnetic interactions ‘escape’ the

<sup>12</sup> Concerning the discrepancy between the present and previous studies of this compound, it is most likely related to a problem with the sample presented in especially [18]. The size of the main magnetic peak and thereby also the effective magnetic moment is clearly smaller in [18] than in our present study. We have carefully confirmed our present results using several different sample batches as well as using a multitude of  $\mu^+$ SR and NPD instruments to ensure the robustness of our current conclusions. In fact the NPD data presented in [18] is most likely instead representative of a sample with significant Ca doping that suppresses the Cr moment [21].

Q1D Cr chains and realize a 2D magnetic structure, developing across the double rutile strings in the *ac*-plane. This observation is also consistent with electronic structure calculations [10], which suggest that such kind of 2D magnetic structure is a very likely ground state for  $\text{NaCr}_2\text{O}_4$ . The absence of geometrical frustration, and the indications of tricritical behavior of the magnetic order parameter, suggest that the spin flop transition observed as a function of external magnetic field [9] could instead be interpreted as metamagnetism.

## 2. Methods

Polycrystalline samples of  $\text{NaCr}_2\text{O}_4$  were prepared from a stoichiometric mixture of  $\text{NaCrO}_2$ ,  $\text{Cr}_2\text{O}_3$ , and  $\text{CrO}_3$  at 1300 °C under a pressure of 7 GPa. The starting materials for the synthesis were the commercially available, high purity (>99%),  $\text{Na}_2\text{CO}_3$ ,  $\text{Cr}_2\text{O}_3$  and  $\text{CrO}_3$ . The samples were synthesized at the National Institute for Material Science in Tsukuba, Japan. The samples were preliminary characterized using in-house x-ray diffraction. This showed that all sample batches were single phase, with a  $\text{CaFe}_2\text{O}_4$ -type *Pnma* structure. Further details on the sample preparation can be found in [11] and [9] (supporting information).

The temperature dependent  $\mu^+$ SR spectra were obtained at the multi purpose surface muon instrument Dolly [23], at the Paul Scherrer Institute in Switzerland [24]. Approximately 500 mg of powder sample was packed in a  $1 \times 1 \text{ cm}^2$  area envelope made from Aluminum-coated Mylar tape (0.05 mm thickness). The envelope was attached to a low background Cu sample holder inserted in a helium exchange gas cryostat (temperature range: 1.6 K to 300 K).

The NPD measurements were performed at the time of flight powder diffractometers iMATERIA [25] and SPICA [26] at the high intensity proton accelerator facility J-PARC, in Japan. The powder samples ( $m \approx 0.72 \text{ g}$ ) were mounted into cylindrical vanadium cells with diameters 6 mm (for SPICA) and 5 mm (for iMATERIA). The cells, sealed using an aluminium cap, aluminium screws and an indium wire, were mounted on a closed cycle refrigerator to reach temperatures between 2 K and 300 K. SPICA and iMATERIA were designed to measure at a single scattering angle while reaching a wide range in reciprocal space using large position sensitive detector banks which could provide different d-ranges (Q-ranges) with gradually changing resolutions. More specifically, in SPICA the high angle detector bank provides a d-range from 0.3 Å up to 3.7 Å (resolution  $\Delta d/d = 0.12\%$ ), while the low angle (LA) detector bank has a d-range from 0.5 Å up to 11 Å. In iMATERIA the backscattering detector bank (BS), allows a d-range from 0.181 Å up to 5.09 Å (resolution  $\Delta d/d = 0.16\%$ ), while the LA detector banks (LA35 and LA15) allow to resolve d-ranges from 0.25 Å up to 40 Å. The high angle banks in SPICA and iMATERIA are therefore suitable for detailed structural characterization, while the LA banks were ideal for identifying any magnetic Bragg peak in the high-d (low-Q) range.

The FullProf suite of programmes [27] was used to determine the crystal and magnetic structure of  $\text{NaCr}_2\text{O}_4$ . The VESTA software [28] was used to produce all the images involving crystal structure. The fitting of the temperature dependent parameters has been performed with the software Igorpro [29], and the *musrfit* [30] software package was used for the  $\mu^+$ SR data treatment.

## 3. Results

In the following section the experimental results with the related data analysis are collected. In the first subsection the temperature dependent  $\mu^+$ SR measurements are presented, while the second subsection shows the NPD measurements for different temperatures.

### 3.1. $\mu^+$ SR Results

The weak transverse field (wTF)  $\mu^+$ SR measurements involve applying an external magnetic field of weak intensity (wTF = 50 G in this case) perpendicular to the initial spin polarization of the muon beam. Such field will cause the muon spin to precess around the direction of the field's flux lines. Measurements in this configuration were carried out in a temperature range  $T = 2 - 145 \text{ K}$  and figure 2(a) shows selected wTF spectra acquired for  $\text{NaCr}_2\text{O}_4$ . At high temperatures, the magnetic moments in the sample are randomly oriented, resulting in a negligible local internal magnetic field compared to the external field that causes the muon spins to precess regularly. Here, the wTF spectra show a cosine-like time dependent trend, with a single frequency related to the value of the external field. As the temperature decreases, the system transitions gradually from the paramagnetic (PM) to the AFM phase. Here, the strong internal AFM field dominates the weak external field, leading to an increase in the overall muon spin depolarization rate and a decrease in the

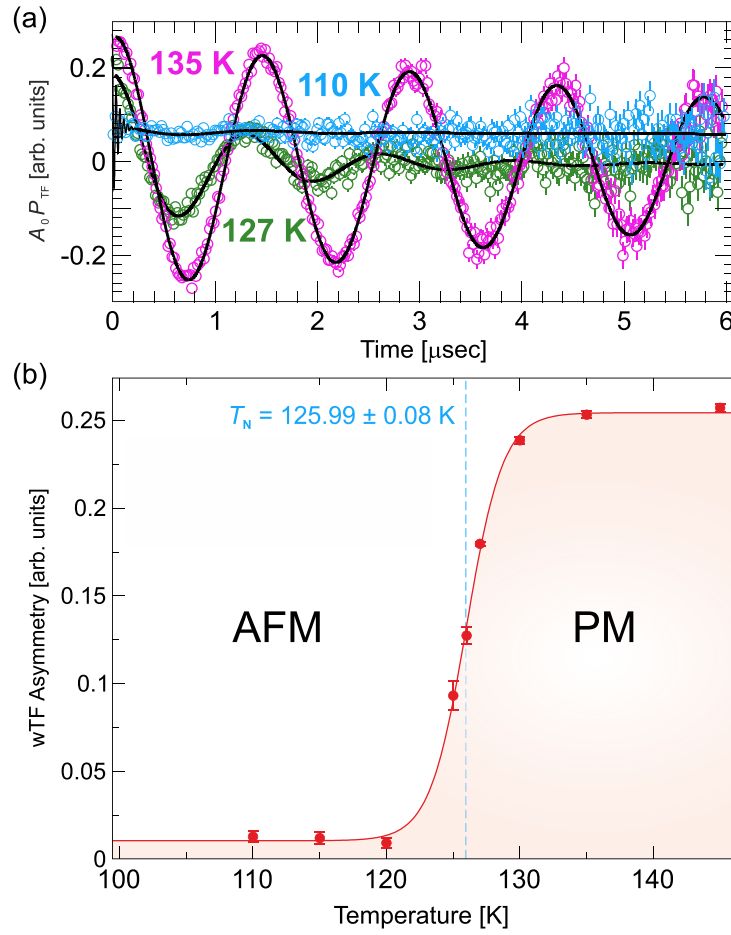


**Figure 2.** (a) Weak transverse field (wTF)  $\mu^+$  SR spectra in the long time domain above the transition temperature for  $\text{NaCr}_2\text{O}_4$ . The spectra are overlapped to show the oscillation around zero asymmetry. (b) The corresponding wTF asymmetry is plotted as a function of temperature, with a fit to a sigmoid curve shown as a solid line. The transition temperature  $T_N \approx 126$  K resulting from the fit is indicated by the vertical dashed line.

amplitude of the wTF oscillations in the spectra. Eventually, only the high frequency oscillations in the early time domain remain (figure 2(a)). The fit function used for the wTF spectra is:

$$A_0 P_{TF}(t) = A_{TF} \cos\left(2\pi \nu_{TF} t + \frac{\pi \phi}{180}\right) \cdot e^{(-\lambda_{TF} t)} + A_{AFM} \cos\left(2\pi \nu_{AFM} t + \frac{\pi \phi}{180}\right) \cdot e^{(-\lambda_{AFM} t)} + A_{tail} \cdot e^{(-\lambda_{tail} t)}. \quad (1)$$

$A_0$  is the initial asymmetry,  $P_{TF}(t)$  is the muon spin polarization function,  $A_{TF}$ ,  $A_{AFM}$  and  $A_{tail}$  are the asymmetries of the related polarization components,  $\nu_{TF/AFM}$  is the frequency of the Larmor precession (whose value is related to the applied wTF and to the internal AFM field respectively),  $\phi$  is the initial phase of the oscillating signal (here zero),  $\lambda_{TF}$ ,  $\lambda_{AFM}$  and  $\lambda_{tail}$  are the depolarisation rates. The magnetic transition temperature can be determined by fitting the temperature dependence of the transverse field asymmetry  $A_{TF}$  to a sigmoid function. Figure 2(b) shows a plot of the wTF asymmetries as a function of temperature. Here an increase in  $A_{TF}$  is observed across the magnetic phase transition, where the system evolves from the low temperature AFM state to the PM state above  $T_N$ . The middle point of the sigmoid fitting curve provides the magnetic transition temperature  $T_N = (125.99 \pm 0.08)$  K.

Inside the AFM phase (e.g. at  $T = 110$  K), the low frequency associated with the wTF is completely suppressed, as clearly seen in the raw data in figure 2. and the signal remains unchanged down to  $T = 2$  K (therefore the  $A_{TF}$  temperature points below 110 K are not shown in the plot). The complete suppression of wTF asymmetry means that the entire sample volume enters the AFM phase. Above  $T_N$ , the wTF asymmetry fully recovers its maximum value, implying that the muons in the entire volume of the sample are precessing according to the weak external field. The smooth transition from full asymmetry to complete suppression of  $A_{TF}$ , without intermediate steps down to base temperature, rules out the possibility of a phase separation and/or substantial magnetic impurities.

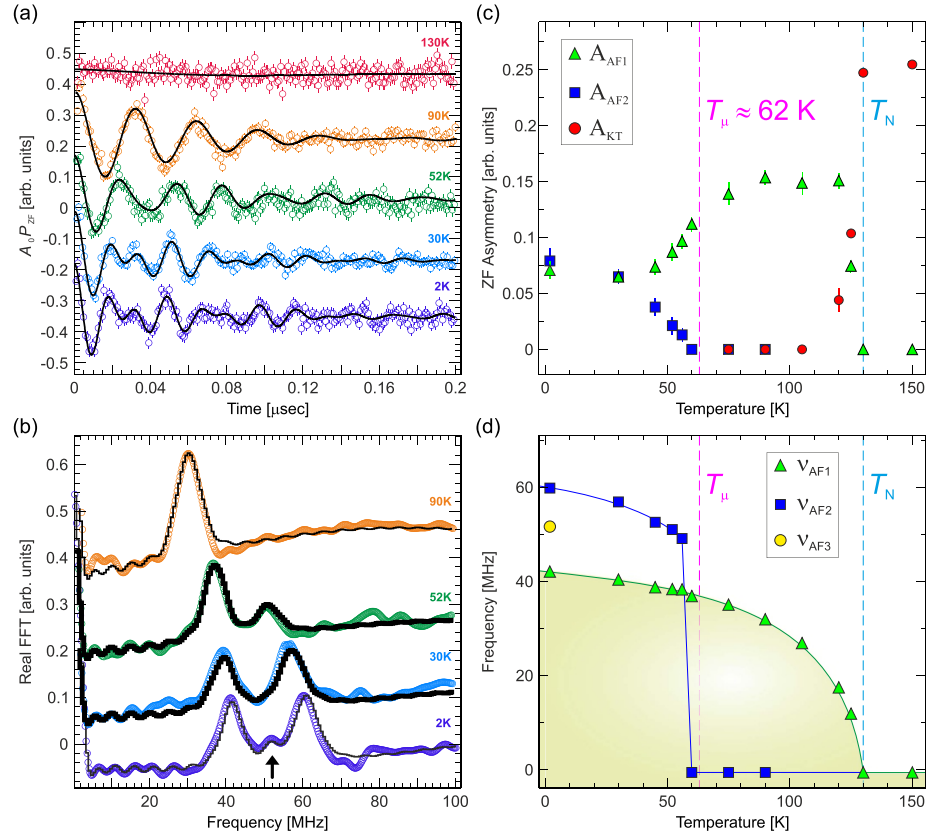
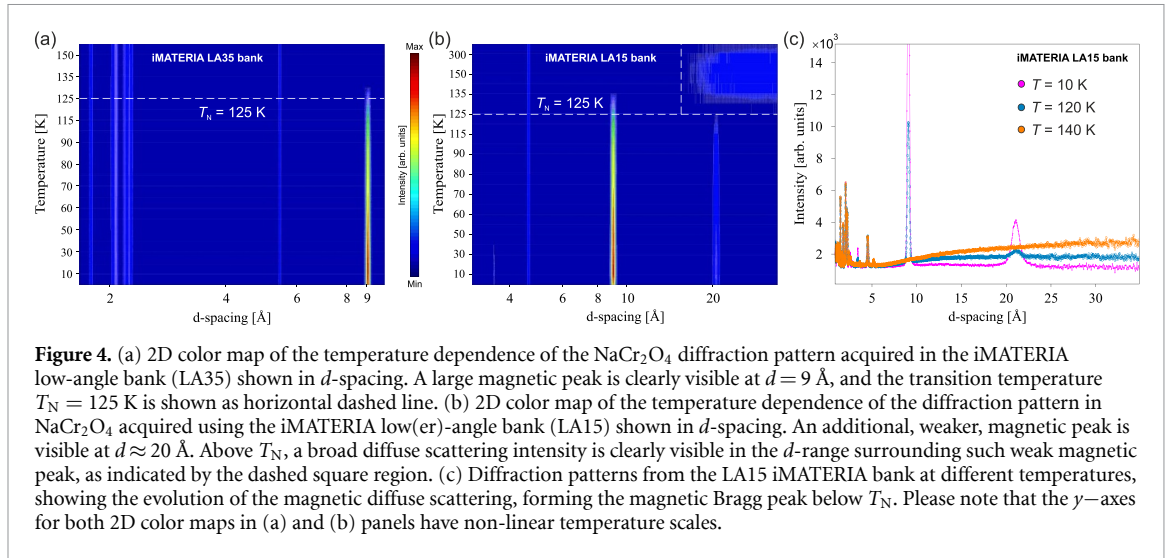


**Figure 3.** (a) Early time domain  $\mu^+$ SR spectra in zero field (ZF) as a function of temperature across the magnetic phase transition revealing an evolution from three to one frequency. The continuous black lines are best fits to the function shown in equation (2). For clarity of display, the spectra have been shifted along the  $y$ -axis. (b) Real part of the fast Fourier transform (FFT) for the NaCr<sub>2</sub>O<sub>4</sub> ZF time spectra displayed in (a), with the continuous black lines again representing fits to equation (2). The black arrow at  $\sim 50$  MHz indicates the third frequency. (c) Temperature dependencies of the asymmetries for the oscillating components of the ZF signal. (d) Temperature dependence of the frequencies of the muon spin Larmor precession. Vertical dashed lines indicate critical temperatures,  $T_\mu \approx 62$  K and  $T_N \approx 130$  K, respectively.

A zero-field (ZF)  $\mu^+$ SR experiment has also been performed for different temperatures, in order to observe the evolution of the internal magnetic field distribution in NaCr<sub>2</sub>O<sub>4</sub>. The muons implanted in the sample act as ultra sensitive microscopic magnetometers, which probe the internal field by following their spin polarization [31]. The resulting ZF  $\mu^+$ SR time spectra for different temperatures in the short time domain are displayed in figure 3(a). In the provided spectra, the distinct patterns observed correspond to the Larmor precession of the muon spins. The angular frequency ( $\omega$ ) of this precession varies in response to the strength of the local magnetic field (with a magnitude of  $B$ ). The time evolution of the muon spin polarization can be accurately modeled by a combination of oscillating functions that exponentially decay over time. At base temperature  $T = 2$  K the fit function chosen for NaCr<sub>2</sub>O<sub>4</sub> is the following:

$$A_0 P_{ZF}(t) = \sum_{i=1,3} A_{AFi} \cos \left( 2\pi \nu_{AFi} t + \frac{\pi \phi_{AFi}}{180} \right) \cdot e^{(-\lambda_{AFi} t)} + A_{tail} \cdot e^{(-\lambda_{tail} t)} + A_{KT} \cdot G_{SGKT}(\Delta, t) \cdot e^{(-\lambda_{KT} t)}. \quad (2)$$

where  $A_0$  is the initial asymmetry of the muon decay,  $P_{ZF}$  is the muon spin polarization function. Here the distinct static internal magnetic field at the muon sites, associated to the commensurate AFM ordering, results in an oscillation of the muon spin polarization (fitted with a cosine function) with three well defined frequencies for the Larmor precession:  $\nu_{AF1} = (41.68 \pm 0.24)$  MHz,  $\nu_{AF2} = (60.95 \pm 0.31)$  MHz and  $\nu_{AF3} = (51.80 \pm 0.31)$  MHz.  $\phi$  is the initial phase of the implanted muon spin polarization. For NaCr<sub>2</sub>O<sub>4</sub> we find that  $\phi \approx 0^\circ$  for all frequencies across the entire temperature range. Further,  $\lambda_{AF}$  is the exponential relaxation rate of the cosine function, and  $A_{tail} \cdot e^{(-\lambda_{tail} t)}$  is the so called ‘tail’ term, related to the components of the internal field that align with the initial polarization direction of the muon spins. This term is commonly found in powder samples.  $G_{SGKT}(\Delta, t)$  is the static Gaussian Kubo-Toyabe relaxation function, commonly used to model the muon spin depolarization in a Gaussian distribution of magnetic fields of width  $\Delta$ , due to the presence of randomly oriented dipole moments (such as in an PM environment) [32, 33].



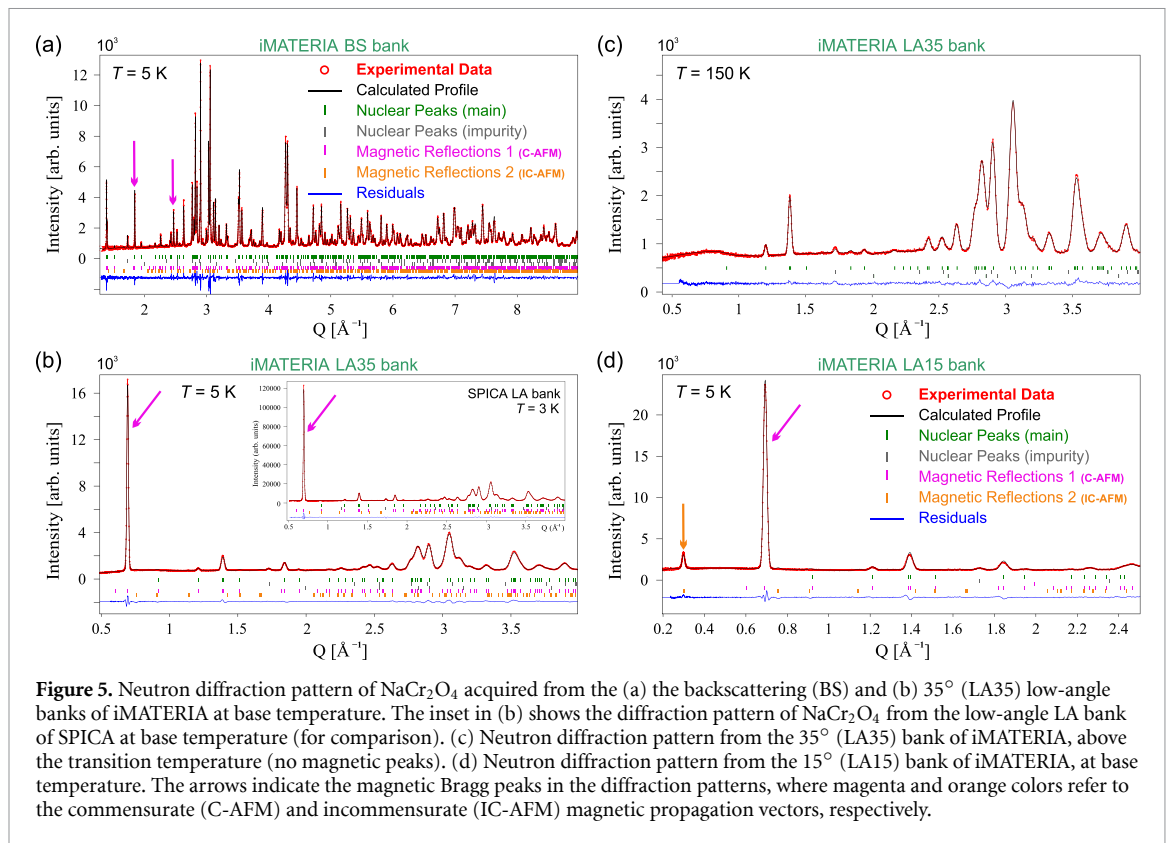
The presence of two clear frequencies is visible in the 2 K muon time spectra and its Fourier transform in figures 3(a) and (b). At this temperature a third frequency could also be included in the fit, however, its small amplitude (compared to the other two frequencies) makes its presence in the muon spectrum questionable. The asymmetries and frequencies of the ZF spectra as a function of temperature are displayed in figures 3(c) and (d). As the temperature increases the spontaneous oscillation of the muon spin polarization, is suppressed until only the SGKT component dominates the spectrum above  $T_N$ . In addition, the asymmetry of the second frequency  $\nu_{AF2}$  undergoes a full suppression for temperatures above  $T_\mu \approx 62$  K (figure 3(d)). Such a drastic change in the frequencies could be related to either a structural phase transition (changing the muon stopping sites) or a change in the spin structure (e.g. spin canting) [34, 35]. However, as we will show below in our detailed NPD study, there is no change in the atomic or magnetic structure occurring in this temperature range. Looking more carefully at the ZF asymmetries in figure 3(c), we see that with increasing temperature, there is a gradual shift of asymmetry from  $A_{AF2}$  to  $A_{AF1}$ . Finally, when crossing  $T_\mu$ , only  $A_{AF1}$  (i.e.  $\nu_{AF2}$ ) survives. Most likely this means that two muon stopping sites are favorable below  $T_\mu$ , but with increasing temperature the second stopping site becomes energetically unfavorable. More detailed computer modeling of the muon stopping sites in  $\text{NaCr}_2\text{O}_4$  will be required to confirm such hypothesis.

### 3.2. NPD Results

To study the temperature evolution of the magnetic structure in  $\text{NaCr}_2\text{O}_4$ , NPD patterns were collected at the time-of-flight (ToF) instrument iMATERIA in J-PARC while comparative low temperature patterns were collected also using the SPICA instrument.

Figures 4(a)–(c) show the temperature evolution of the diffraction pattern in the high- $d$  (low- $Q$ ) range. Here, the absence of splitting for the nuclear Bragg peaks in the low- $d$  range, indicates that no structural transitions occur in the investigated temperature range (figure 4(a)). A high-intensity magnetic peak (and several other), appearing at  $T_N = 125$  K, is clearly seen at  $d = 9$  Å, as expected from previous characterizations. In addition, a weaker magnetic peak appears at even higher  $d \sim 20$  Å for  $T < T_N$ . These two magnetic reflections manifest a slightly different phenomenology. Indeed, in the  $d$ -range around 20 Å, a broad diffuse scattering intensity is clearly visible above  $T_N$  (inside the dashed rectangle in figure 4(b)), while no such scattered intensity can be observed around  $d = 9$  Å. The diffuse scattering indicates the presence of short-range spin correlations in the temperature range between 130 K and 300 K. Below 130 K, such disordered state is replaced by a long range magnetic order, and the diffuse scattered intensity condenses into a magnetic Bragg peak at  $d \sim 20$  Å (figure 4(c)). The presence of high-temperature short range magnetic correlations in  $\text{NaCr}_2\text{O}_4$  was never reported before. Indeed, no anomalies have been observed in any of the bulk magnetic measurements on this material in the temperature range where the diffuse scattering appears. Nevertheless, it should be mentioned that the Curie constant measured in  $\text{NaCr}_2\text{O}_4$  was found to be significantly smaller than the theoretical one [11]. This unexpected value was interpreted and explained with the presence of large quantum fluctuations due to spin frustration. Since we can exclude the hypothesis of spin frustration in  $\text{NaCr}_2\text{O}_4$ , we might associate the small value of the Curie constant to the presence of short-range magnetic correlations. However, additional studies would be needed to further investigate this high temperature diffuse scattering. The behavioral difference between the strong and the weak magnetic





peaks suggests that they are originated by two distinct periodic arrangements of the magnetic moments in the Cr lattice.

In order to determine the magnetic and crystal structure of  $\text{NaCr}_2\text{O}_4$  with high confidence, the diffraction data from all the 4 ToF detector banks were simultaneously analyzed with a global Rietveld refinement (see Methods section for the description of the detector banks) while keeping as common parameters the  $a$ ,  $b$  and  $c$  axes, the atomic positions and the basis vectors of the magnetic moment. A comparative refinement for data collected in one of the LA banks from SPICA at  $T = 3$  K was used as additional confirmation and provided very similar results. The low temperature refined profiles with the experimental data from both instruments measured with different detector banks are displayed in figures 5(a)–(d), where the magnetic peaks are highlighted by magenta and orange arrows. The observed profiles are in very good agreement with the calculated models, as also underlined by the low values of the reliability R-factors, reported in table 1 along with refined structural parameters at both high and low temperature.

The calculated diffraction pattern contains a nuclear and a two magnetic  $\text{NaCr}_2\text{O}_4$  phases, plus two small impurity phases:  $\text{Cr}_2\text{O}_3$  (a Mott-Hubbard AFM insulator with the Néel temperature  $T_N = 307$  K) and  $\text{CrO}_2$  (an FM half metal with a Curie temperature of 390 K). The weight fractions for these impurities in the diffraction pattern correspond to 2.16% for  $\text{Cr}_2\text{O}_3$  and to 0.42% for  $\text{CrO}_2$ . The high and low temperature nuclear phase was found to be well modeled by a orthorhombic  $Pnma$  space group (No. 62), in agreement with previously reported results. In our high-resolution data we also found that the adoption of strain parameters (only relevant for the high resolution BS bank pattern) substantially improved the refinement in the full temperature range. The strain is probably a heritage of the high pressure synthesis process necessary to manufacture the sample. The Rietveld refinement of the  $\text{NaCr}_2\text{O}_4$  magnetic phases includes the two magnetic Cr atoms in their respective crystallographic sites. The scale factors and structural parameters were constrained to be equal to their counterparts in the nuclear  $\text{NaCr}_2\text{O}_4$  phase, for a proper estimation of the Cr moments  $\mu_{\text{Cr}}$  in the two magnetic cells. The indexing of the temperature dependent magnetic Bragg reflections was achieved with the magnetic propagation vectors  $k_1 = (1\ 0\ 1)$  and  $k_2 = (0\ 0\ 0.497) = (0\ 0\ \frac{1}{2} - \delta)$ , determined with the software K-Search. While the  $k_1$  magnetic cell is commensurate (C-AFM) to the crystal structure, the  $k_2$  cell is IC (IC-AFM) and has the  $c$ -axis doubled with respect to the nuclear and  $k_1$  magnetic cells (see also figure 6).



**Table 1.** Structural lattice parameters, atomic positions and isotropic thermal displacement parameters ( $B_{\text{iso}}$ ) for  $\text{NaCr}_2\text{O}_4$ , as refined from neutron powder diffraction data (iMATERIA, global fit to all detector banks). Also shown are the refinement reliability factors for the nuclear [ $R_{\text{B(nuc)}}$ ] and magnetic [ $R_{\text{B(mag1)}}$ ] and [ $R_{\text{B(mag2)}}$ ] phases, as well as the global  $\chi^2$  for the four detector banks. All the atomic positions have the site symmetry  $4c$ .

	$T = 300 \text{ K}$	$T = 5 \text{ K}$
Space Group	$Pnma$	$Pnma$
$a$ ( $\text{\AA}$ )	9.01 556(5)	9.0305(1)
$b$ ( $\text{\AA}$ )	2.91 279(1)	2.91 695(3)
$c$ ( $\text{\AA}$ )	10.41 412(6)	10.3428(1)
$\alpha = \beta = \gamma$	$90^\circ$	$90^\circ$
Na (x, y, z)	(0.243(2), 1/4, 0.347(1))	(0.244(2), 1/4, 0.348(1))
Cr1 (x, y, z)	(0.082(1), 1/4, 0.603(1))	(0.083(2), 1/4, 0.603(1))
Cr2 (x, y, z)	(0.063(1), 1/4, 0.114(1))	(0.062(2), 1/4, 0.115(1))
O1 (x, y, z)	(0.2958(8), 1/4, 0.6489(7))	(0.297(1), 1/4, 0.6499(8))
O2 (x, y, z)	(0.3860(8), 1/4, 0.9803(7))	(0.3867(9), 1/4, 0.9805(9))
O3 (x, y, z)	(0.4768(9), 1/4, 0.2170(7))	(0.476(1), 1/4, 0.2177(9))
O4 (x, y, z)	(0.0756(9), 1/4, 0.9295(8))	(0.074(1), 1/4, 0.9287(8))
$B_{\text{iso}}(\text{Na})$ ( $\text{\AA}^2$ )	0.503(5)	0.39(2)
$B_{\text{iso}}(\text{Cr1})$ ( $\text{\AA}^2$ )	0.058(9)	0.025(8)
$B_{\text{iso}}(\text{Cr2})$ ( $\text{\AA}^2$ )	0.093(3)	0.18(2)
$B_{\text{iso}}(\text{O1})$ ( $\text{\AA}^2$ )	0.121(1)	0.09(1)
$B_{\text{iso}}(\text{O2})$ ( $\text{\AA}^2$ )	0.165(1)	0.14(2)
$B_{\text{iso}}(\text{O3})$ ( $\text{\AA}^2$ )	0.147(1)	0.23(1)
$B_{\text{iso}}(\text{O4})$ ( $\text{\AA}^2$ )	0.207(1)	0.19(2)
$R_{\text{B(nuc)}} (\%)$	3.64	2.98
$R_{\text{B(mag1)}} (\%)$	—	0.802
$R_{\text{B(mag2)}} (\%)$	—	7.14
Global $\chi^2$	6.4	10

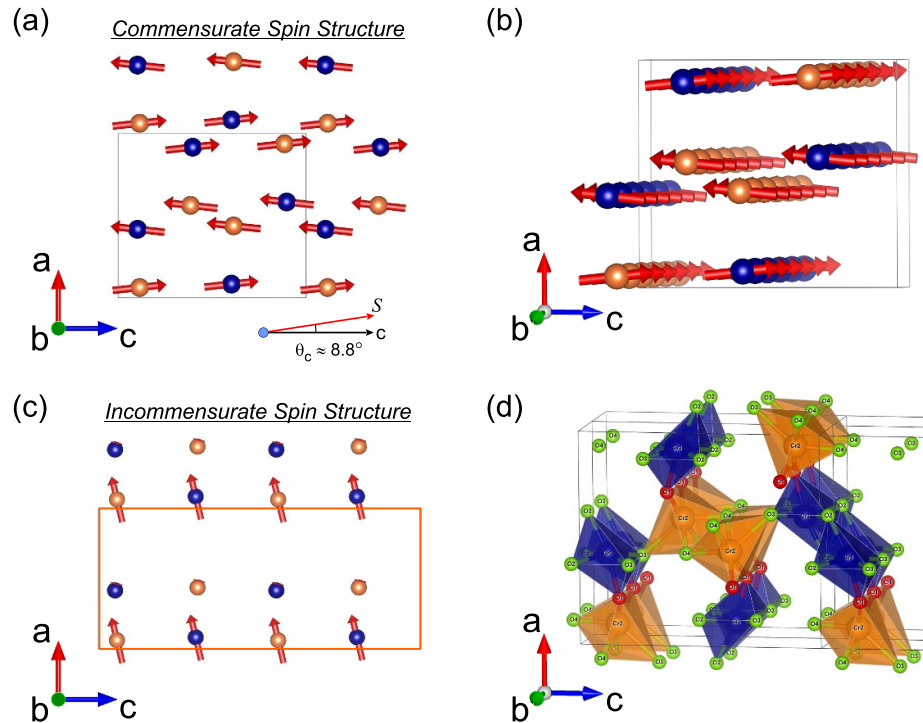


**Figure 6.** (a), (b) Commensurate (C-AFM) spin structure of  $\text{NaCr}_2\text{O}_4$  with  $k_1 = (1\ 0\ 1)$  at  $T = 5 \text{ K}$ . The Na atoms have been removed for clarity of display. The spin canting [ $\theta_c \approx (8.8 \pm 0.5)^\circ$ ] and the AFM coupling of the chains along the  $a$ -axis is visible from the  $ac$ -plane orientation. The ferromagnetic alignment of the Cr spin within the chains along the  $b$ -axis is emphasized in the (b) panel. (c) Incommensurate (IC-AFM) magnetic supercell with  $k_2 = (0\ 0\ \sim 1/2)$ . The spin alignment in this case is cycloidal, but a systematic suppression of the anti-parallel Cr moments along the  $a$ -axis also occurs. (d)  $\text{CrO}_6$  octahedra with the oxygen sites explicitly labelled. The oxygen site (O1) that mediates the AFM coupling between the zig-zag Cr chains is highlighted in red.

**Table 2.** Basis vectors of the irreducible representations  $\Gamma_7(k_1)$  and  $\Gamma_4(k_2)$  of the magnetic propagation vector group  $G_k$ .

$\Gamma_7(k_1)$ : C-AFM		
SYMM	x,y,z	
BsV <sub>1</sub> (Re)	(1 0 0)	(0 0 1)
BsV <sub>1</sub> (Im)	(0 0 0)	(0 0 0)
SYMM	$-x+1/2, -y, z+1/2$	
BsV <sub>2</sub> (Re)	(1 0 0)	(0 0 -1)
BsV <sub>2</sub> (Im)	(0 0 0)	(0 0 0)
SYMM	$-x, y+1/2, -z$	
BsV <sub>3</sub> (Re)	(1 0 0)	(0 0 1)
BsV <sub>3</sub> (Im)	(0 0 0)	(0 0 0)
SYMM	$x+1/2, -y+1/2, -z+1/2$	
BsV <sub>4</sub> (Re)	(1 0 0)	(0 0 -1)
BsV <sub>4</sub> (Im)	(0 0 0)	(0 0 0)
$\Gamma_4(k_2)$ : IC-AFM		
SYMM	x,y,z	
BsV <sub>1</sub> (Re)	(1 0 0)	(0 0 1)
BsV <sub>1</sub> (Im)	(0 0 0)	(0 0 0)
SYMM	$-x+1/2, -y, z+1/2$	
BsV <sub>2</sub> (Re)	(-0.022 0 0)	(0 0 0.022)
BsV <sub>2</sub> (Im)	(-1 0 0)	(0 0 1)

The software BasIreps provided the possible irreducible representations of the propagation vector group  $G_k$  compatible with the space group  $Pnma$  and the propagation vectors  $k_1$  and  $k_2$ . The direct sum of 8 possible irreducible representations (IRrep) gave the reducible representation for  $k_1$  as  $\Gamma = 1\Gamma_1 \oplus 2\Gamma_2 \oplus 2\Gamma_3 \oplus 1\Gamma_4 \oplus 1\Gamma_5 \oplus 2\Gamma_6 \oplus 2\Gamma_7 \oplus 1\Gamma_8$ . Among the different IRreps used to refine the magnetic phase with a trial and error approach, the  $\Gamma_7$  of dimension 1 contained 2 times in  $\Gamma$  was selected as the one that could provide the best match. For  $k_2$  the reducible representation can be written as  $\Gamma = 1\Gamma_1 \oplus 2\Gamma_2 \oplus 1\Gamma_3 \oplus 2\Gamma_4$ . Among the different IRreps used to refine the magnetic phase with a trial and error approach, the  $\Gamma_4$  of dimension 1 contained 2 times in  $\Gamma$  was selected as the one that could provide the best match. Table 2 reports the real and imaginary basis vectors of the  $\Gamma_7(k_1)$  and  $\Gamma_4(k_2)$  representation for the crystallographic symmetry operators associated with the two Cr sites (Cr1 and Cr2).

The coefficients of these basis vectors for both  $k_1$  and  $k_2$ , namely C1 and C2, were refined as common parameters for both the Cr sites, since no significant improvement for the refinement was observed by leaving them independent. The resulting spin axial vector for  $k_1$  has a large component along the crystallographic  $c$ -direction, a smaller component along the  $a$ -direction and zero component along the  $b$ -direction, leading to a tilt of the Cr spin with respect to the  $c$ -axis. Due to the presence of imaginary basis vectors for the IRrep of  $k_2$ , the resulting spin axial vector has a cycloidal-like modulation along the  $a$ -axis, reminiscent of the magnetic structure found in the isostructural compound  $\text{NaMn}_2\text{O}_4$  [6]. The latter material also exhibits two distinct C-AFM and IC-AFM magnetic cells. However, while in  $\text{NaMn}_2\text{O}_4$  the AFM coupling and the IC modulation of the Mn moments develop along the zigzag Mn chains, in  $\text{NaCr}_2\text{O}_4$  the magnetic structures develop along the rutile chains in the  $ac$ -plane. As a result, the C-AFM alignment of the Cr spins exhibits canting, and the IC cycloidal Cr spin arrangement display systematic suppression of the Cr moment on the spin inversion sites. A graphic representation of the obtained magnetic structures is displayed in figures 6(a)–(c). For the  $k_1$  cell, the canted AFM coupled FM double rutile chain along the  $c$ -axis, are clearly visible in figure 6(a), while the FM zig-zag chains running along the  $b$ -axis are emphasized in figure 6(b). For the  $k_2$  cell, the modulated cycloidal arrangement of the Cr moments along the  $a$ -axis is displayed in figure 6(c). Figure 6(d) explicitly shows the different Cr and O sites in the lattice, including the oxygen site (O1) that mediates the AFM coupling between the zig-zag Cr chains.

For the  $k_1$  structure, the canting angle  $\theta_c = (8.8 \pm 0.5)^\circ$ , was estimated from the average value of the components of the basis vector C1 and C2 through the temperature range from base-T to 100 K. This angle is obtained with higher confidence with respect to the one reported previously  $(8.1 \pm 7.3)^\circ$  [18]. The total moment of the Cr atoms, calculated as the modulus of the Cr spin axial vector averaging among the low

temperature fluctuations, is  $\mu_{\text{Cr}}^{\text{C}} = (4.30 \pm 0.01)\mu_{\text{B}}$  for the  $k_1$  structure, and  $\mu_{\text{Cr}}^{\text{IC}} = (2.20 \pm 0.03)\mu_{\text{B}}$  for the  $k_2$  structure.

#### 4. Discussion

The  $\mu_{\text{Cr}}^{\text{C}}$  value found in this work is remarkably higher than the expected spin only value for a system with a nominal valence state  $\text{Cr}^{3.5+}$ , since  $S_{\text{Cr}^{3+}} = 3.87 \mu_{\text{B}}$  and  $S_{\text{Cr}^{4+}} = 2.83 \mu_{\text{B}}$  (which are actually consistent with  $\mu_{\text{Cr}}^{\text{IC}}$ ). Values closer to the measured  $\mu_{\text{Cr}}^{\text{C}}$  value could be achieved by including the orbital contributions to the total Cr moment, which would sum up to a moment of 5.2 and 4.5  $\mu_{\text{B}}$  for  $\text{Cr}^{3+}$  and  $\text{Cr}^{4+}$ , respectively. However, orbital contributions from Cr in an octahedral environment is expected to give negligible contribution to the total moment. This is due to orbital quenching in a crystal field [36], making this option less probable. Indeed, even though orbital contributions of vanadium in octahedral environment was in fact recently suggested in  $\text{VI}_3$  by  $\mu^+$ SR and XAS [37, 38], for  $\text{NaCr}_2\text{O}_4$ , an unusual mixed valence electronic state has instead been reported [8]. It was suggested that Na substitution in the solid solution  $\text{Na}_x\text{Ca}_{1-x}\text{Cr}_2\text{O}_4$  does not result in electrons removed from the Cr site, as expected in typical mixed valence compounds. Here, the electrons are instead removed from the O sites, to relax charge frustration and realize a negative charge transfer state [8]. In fact, the large value of the Cr moment ( $\mu_{\text{Cr}}^{\text{C}}$ ) measured in this work could be explained by the negative charge transfer state induced in  $\text{NaCr}_2\text{O}_4$ , since it could lead to a Cr valence  $\text{Cr}^{2+}$  in a high spin state  $d^3$  ( $t_{2g}^3 e_g^1$ ). The expected spin only value for  $\text{Cr}^{2+}$  is 4.9  $\mu_{\text{B}}$ , which is comparable to  $\mu_{\text{Cr}}^{\text{C}}$ . Therefore, our results could indirectly confirm the unusual charge transfer state present in  $\text{NaCr}_2\text{O}_4$  [8]. While it was not commented on, since CO is not observed in this system [10, 14], this kind of electronic configuration also suggest highly fluctuating vacancies. A similar situation was also observed for the 1D mixed valence system  $\text{K}_2\text{Cr}_8\text{O}_{16}$  [39], which is structurally analogous to  $\text{NaCr}_2\text{O}_4$ .

Additionally, our result is consistent with the predictions of recently published DFT calculations [22], which envision a spin disproportionation between the Cr1 and Cr2 sites. This would lead to the existence of high-spin Cr sites in the magnetic ground state of  $\text{NaCr}_2\text{O}_4$ . The authors of [22] evaluated the modulus of the Cr moment as  $\approx 2\mu_{\text{B}}$  for both low and high spin states, which is close to the value found in [18]. Nevertheless, they also acknowledge that, due to the uncertainty of the results of [18], their estimation cannot be experimentally validated. The large value of  $\mu_{\text{Cr}}^{\text{C}}$  obtained in this work is also consistent with a magnetic coupling mechanism mediated by ligand holes in  $\text{NaCr}_2\text{O}_4$ , as also suggested in [8, 11]. This aspect will be further expanded below in the discussion related to the coupling mechanism involved in the magnetic order.

The temperature dependence of the structure factor  $F[0\ 0\ -1]$ , obtained as the square root of the integrated intensity of the large  $k_1$  magnetic peak ( $0\ 0\ -1$ ) and smaller  $k_2$  magnetic peak ( $0\ 0\ 0$ ), are plotted in figure 7(a). The solid lines are fits to the power law:

$$f(x) \propto \left(1 - \frac{x}{T_c}\right)^{\beta}. \quad (3)$$

The temperature evolution of the diffraction peak is related to the order parameter of the magnetic phase transition. By fitting it with equation (3) it is possible to estimate the onset of the magnetic transition temperature, and acquire some indications about the type of symmetry breaking that the system undergoes. The onset of the magnetic transition was found at  $T = (130 \pm 0.003)$  K, in good agreement with the  $\mu^+$ SR measurements. The value of the critical exponent, estimated for the  $k_1$  peak, was found  $\beta_1 = 0.245 \pm 0.007 \approx \frac{1}{4}$ , suggesting that the AFM-PM phase transition in  $\text{NaCr}_2\text{O}_4$  is located at a tricritical point [40]. Within the Landau mean-field approximation, this means that the onset of the magnetic transition in  $\text{NaCr}_2\text{O}_4$  is a point between the edge of a second order transition and the ordinary critical point of a first-order transition [41, 42]. The tricritical behavior observed in this work, together with the dramatic increase in the magnetization with the relatively small externally applied field of 3.5 T (associated to a spin-flop transition) [9], are compatible with the fact that a possible hidden metamagnetic state [43] is established in this material at the edge of the AFM-PM transition. This conjecture is based on the qualitative agreement between  $\text{NaCr}_2\text{O}_4$  and tricritical metamagnetic systems that manifest a similar phenomenology, i.e.  $\text{NiCl}_2 \cdot 2\text{H}_2\text{O}$ ,  $\text{Ni}(\text{NO}_3)_2$  [44–46]. In these systems, magnetic field dependent changes in magnetization and susceptibility were erroneously identified as spin-flop transitions. Nevertheless, studies of the evolution of the magnetic structure under high magnetic fields would be necessary to resolve the ambiguity of the field induced transitions, and to outline of the magnetic phase diagram of  $\text{NaCr}_2\text{O}_4$ . The temperature dependencies of both the coefficients of the  $k_1$  basis vectors C1, C2 follow the same trend as the structure factor  $F[0\ 0\ -1]$  (cf figures 7(a) and (b)), suggesting that the canting angle of the Cr spin axial vector is maintained across the full temperature range, as its modulus decreases. The temperature trend for the

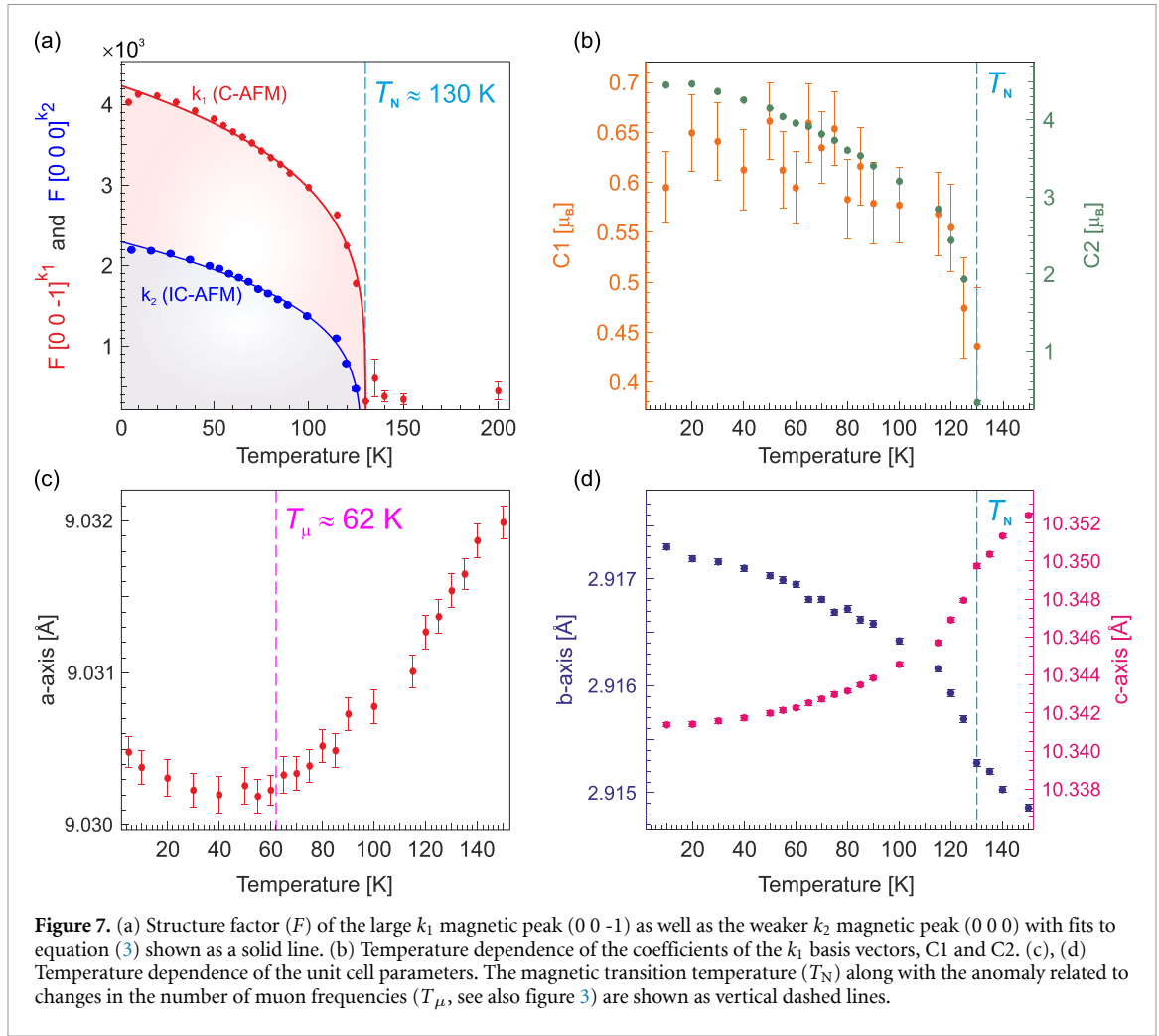


**Figure 7.** (a) Structure factor ( $F$ ) of the large  $k_1$  magnetic peak (0 0 -1) as well as the weaker  $k_2$  magnetic peak (0 0 0) with fits to equation (3) shown as a solid line. (b) Temperature dependence of the coefficients of the  $k_1$  basis vectors,  $C1$  and  $C2$ . (c), (d) Temperature dependence of the unit cell parameters. The magnetic transition temperature ( $T_N$ ) along with the anomaly related to changes in the number of muon frequencies ( $T_\mu$ , see also figure 3) are shown as vertical dashed lines.

structure factor  $F[0\ 0\ 0]$  of the  $k_2$  magnetic peak is also displayed in figure 7(a). Here the critical exponent is estimated as  $\beta_2 = 0.31 \pm 0.01$ , which is close to the value for a 3D Heisenberg AFM with a 1-dimensional order parameter [40], suggesting a more conventional magnetic ground state for this phase.

The temperature dependence of the unit cell parameters are displayed in figures 7(c) and (d). On cooling, the value of the  $a$ -axis decreases monotonically down to  $T \approx 60$  K, where an inversion of trend is observed. Phenomenologically, such inversion coincides with the suppression of the second muon frequency at  $T_\mu \approx 62$  K. This could be a weak indication that the subtle changes in the lattice could yield an energetically unfavorable situation for one of the muon stopping sites. The value of the  $b$ -axis instead increases monotonically, with a trend similar to the one observed for the evolution of the magnetic parameters in figures 7(a) and (b), with a clear change in slope at the magnetic transition temperature  $T_N = 125$  K. The  $c$ -axis undergoes a monotonic decrease down to base temperature, with a similar but mirrored behavior as the one observed in the  $b$ -axis. The temperature evolution of the unit cell parameters shows evidence of coupling between the crystal and magnetic structure. However, since the magnetic ordering does not induce a structural transition towards a different lattice symmetry, but only very slight changes in the lattice parameters, such coupling does not seem to be very strong. Finally, the  $\mu^+$ SR precession signal displayed a gradual transition from two to one frequency at  $T_\mu \approx 62$  K (figure 3(b)). As already mentioned above, since no dramatic effect is present in the NPD patterns (neither nuclear nor magnetic) around these temperatures (figure 7), the reason for the change in the frequency spectrum is probably due to a change in the structural muon sites. Here the temperature evolution of the lattice and atomic positions could simply result in that one of the muon stopping site becomes energetically unfavorable above  $T_\mu$ .

It appears that, depending on the reciprocal orientation of the octahedra, FM and AFM exchange interaction are established between the Cr ions. In particular, for the  $k_1$  magnetic structure, three different magnetic couplings seem to be in place below  $T_N$ : ① An inter-chain FM exchange mechanism is always established across the edge sharing octahedra in the Cr1 and Cr2 chains. ② An intra-chain FM exchange mechanism is always established across the corner sharing octahedra between the chains stacked along the

$c$ -direction (through the oxygen atom in the crystallographic site O3). ③ an intra-chain AFM coupling is always established across corner sharing octahedra between the chains stacked along the  $a$  direction (through the oxygen atom in the crystallographic site O1). Consistently with the large value of the Cr moment extracted in this work, we can consider the ligand holes concentrated at the corner oxygen O1 and O3 sites [10] as the main responsible for the occurrence of the C-AFM phase  $k_1$ . Using the arguments similar to the ones presented in [47], the FM inter-chain coupling can be indeed interpreted in terms of a double exchange FM mechanism mediated by the hopping of the O3 ligand holes. This would involve Cr orbitals with one localized electron per site and one with itinerant character, through the bond  $Cr1 - \widehat{O3} - Cr2$ . In fact, the O ions on the edges shared by the octahedra in the zig-zag double chain (O2, O4), were found to give insignificant contributions to the bands near the Fermi level [10]. Therefore, the observed inter-chain FM coupling can be considered a consequence of the intra-chain FM double exchange. This is compatible with the temperature evolution of the crystal structure, in which a monotonic increase of the  $b$ -axis on cooling suggests an increase of the Cr-Cr distances within the zig-zag double chain (i.e. compatible with a Coulomb repulsion effect). A similar phenomenology was observed in other systems such as  $K_2Cr_8O_{16}$  and  $CrO_2$  [2, 47–49].

Despite the dominance of FM double-exchange interaction, intra-chain AFM coupling is established along the  $c$ -axis double rutile chains. It has been suggested that the AFM coupling is due to a weak super-exchange coupling through the bond  $Cr1 - \widehat{O1} - Cr2$  [18]. However, it can naively be argued that an AFM super-exchange interaction across a  $Cr - \widehat{Anion} - Cr$  bond requires a bond angle of  $180^\circ$  [50]. Cases in which the AFM super-exchange mechanism occurs across bond angles that deviate from  $180^\circ$  can of course be realized in the presence of complex crystal-field symmetries of the magnetic ions (like in our case, with the distorted octahedral coordination of Cr ions). However, in  $NaCr_2O_4$  the value of the bond angle  $Cr1 - \widehat{O1} - Cr2 = 125.58(5)^\circ$ , is very far from  $180^\circ$  (is actually closer to  $90^\circ$ , which would favor FM coupling not AFM). Therefore we suggest the mutual hopping of 2 itinerant electrons between the two Cr sites, aided by the O1 ligand holes, as a possible alternative mechanism to explain the intra-chain AFM coupling in  $NaCr_2O_4$ . The hopping of correlated itinerant electrons was suggested as a possible mechanism to explain the magnetic ordering in  $CrO_2$  [47]. Such suggestion was though discarded since it would have lead to AFM ordering, which is not observed in  $CrO_2$ . Since the  $Cr1 - \widehat{O1} - Cr2$  and  $Cr1 - \widehat{O3} - Cr2$  bonds are structurally equivalent and the O1 and O3 sites are both preferred for the localization of the ligand holes, a similar hopping coupling mechanism would be expected. The only difference between the two bonds would be the mutual orientation of the electronic orbitals in the non-equivalent Cr sites. Here, the different distortions between  $Cr1O_6$  and the  $Cr2O_6$  octahedra, remove the degeneracy of the Cr- $3d$  orbitals, leading to one localized and two itinerant orbitals for the Cr1 site, and two localized and one itinerant orbital for the Cr2 site [10]. Due to the lack of inversion symmetry between Cr ions, the canting of the moments in this spin configuration is consistent with an anisotropic AFM exchange including an antisymmetric Dzyaloshinsky-Moriya exchange term [51, 52].

The proposed correlated electron hopping mechanism for the AFM coupling is deduced as a logic consequence of these observations. In this regard, given the discrepancy between the estimated moduli of the moments for the two C-AFM and IC-AFM structures (i.e.  $\mu_{Cr}^C = 4.3 \mu_B$  vs.  $\mu_{Cr}^{IC} = 2.2 \mu_B$ ), and the different values of their critical exponents  $\beta_1 \sim \frac{1}{4}$  and  $\beta_2 \sim 0.31$ , we suggest that the itinerant hopping electrons are responsible for the  $k_1$  long-range C-AFM order, while the localized electrons are responsible for the IC-AFM order. To verify this conjecture, neutron diffraction studies under applied magnetic fields would be an optimal and direct test. Indeed, magnetic structures with itinerant character are sensitive to external magnetic fields, while the localized ones are not [53]. Early stage investigations in this direction are currently ongoing in relation to the present work, and preliminary magnetic field dependent neutron diffraction measurements on  $NaCr_2O_4$  (here not shown) already seem to confirm our conjecture about the dual itinerant/localized nature of the magnetic structure in this material. Indeed, in these measurements, the magnetic peaks belonging to the C-AFM structure are found to be heavily affected by the presence of the magnetic field while the peaks belonging to the IC-AFM structure are not. Such studies will be relevant to discern the effects of the localized and itinerant electrons on the Cr moment, and clarify the magnetic (H/T) phase diagram of  $NaCr_2O_4$ .

## 5. Conclusions

The detailed and partly revised magnetic structure of  $NaCr_2O_4$  is presented in this work. The analysis of high-resolution data shed new light on this interesting compound. In addition to a canted C-AFM phase with propagation vector  $k_1 = (1\ 0\ 1)$ , an additional IC cycloidal-like magnetic phase is identified with propagation vector  $k_2 = (0\ 0\ \frac{1}{2} - \delta)$ . Following the temperature evolution of the structure factor of the



magnetic reflections, indications of unconventional critical behavior for the  $k_1$  magnetic phase transition in  $\text{NaCr}_2\text{O}_4$  were found. In particular, we suggest that the magnetic transition might be at the edge of a tricritical point with possible formation of a metamagnetic hidden phase. Weak interplay between the crystal and magnetic structure, evidenced by the comparison between the  $\mu^+$ SR and NPD data, is compatible with the absence of geometric frustration. The value of the effective Cr moments of the C-AFM and IC-AFM structures were extracted as  $\mu_{\text{Cr}}^{\text{C}} = 4.3 \mu_{\text{B}}$  and  $\mu_{\text{Cr}}^{\text{IC}} = 2.2 \mu_{\text{B}}$ , respectively. The high  $\mu_{\text{Cr}}^{\text{C}}$  value is consistent with a double exchange coupling mechanism mediated by itinerant Cr moments (i.e. the ligand-hole hopping mechanism), for the  $k_1$  C-AFM order. On the other hand, the lower  $\mu_{\text{Cr}}^{\text{IC}}$  value is consistent with a coupling mechanism mediated by exchange interactions between localized Cr spins, for the  $k_2$  IC order. The value of the canting angle of the Cr spin axial vector for the C-AFM structure has been determined with high accuracy as  $\theta_c = (8.8 \pm 0.5)^\circ$ . A FM double-exchange interaction, together with an AFM correlated itinerant electrons hopping interaction, have been proposed as the mechanisms driving the magnetically ordered  $k_1$  phase in  $\text{NaCr}_2\text{O}_4$ .

## Data availability statement

All data that support the findings of this study are included within the article (and any supplementary files).

## Acknowledgment

The  $\mu^+$ SR measurements were performed at instrument *Dolly* of the Swiss Muon Source ( $\text{S}\mu\text{S}$ ), at the Paul Scherrer Institute in Villigen, Switzerland. The NPD measurements were performed at the instruments iMATERIA and SPICA of the neutron spallation source J-PARC (beamtime proposals: 2019A0330, 2019B0420). The authors wish to thank Dr Hiroshi Nozaki for his valuable help during the  $\mu^+$ SR experiment along with the staff of PSI and J-PARC for their great support during the  $\mu^+$ SR and NPD experiments. In particular we wish to thank the late Dr Jean-Christophe Orain, instrument scientist at *Dolly*, who greatly contributed to the  $\mu^+$ SR results here presented.

This research is funded by the Swedish Foundation for Strategic Research (SSF) within the Swedish national graduate school in neutron scattering (SwedNess), as well as the Swedish Research Council VR (Dnr. 2021-06157 and Dnr. 2017-05078), and the Carl Tryggers Foundation for Scientific Research (CTS-18:272). J S is supported by the Japan Society for the Promotion Science (JSPS) KAKENHI Grant Nos. JP18H01863 and JP20K21149. Y S and O K F are supported by the Swedish Research Council (VR) through a starting Grant (Dnr. 2017-05078). Y S acknowledges the funding from the Area of Advance-Materials Sciences from Chalmers University of Technology.

## Author contributions statement

E N, J S, and M M conceived the experiments. E N, O K F, N M, F M, A Z, A H, D A, J-C O, T S, I U, Y S, J S and M M conducted the experiments. E N, O K F, J S, N M, and M M analyzed the results. The samples were synthesized by H S, who also conducted the initial sample characterizations. E N and M M made all the figures. E N created the first draft, and all co-authors reviewed and revised the manuscript.

## Conflict of interest

The authors declare no competing interests.

## ORCID iDs

Elisabetta Nocerino  <https://orcid.org/0000-0003-4441-8882>

Yasmine Sassa  <https://orcid.org/0000-0003-1416-5642>

## References

- [1] Adler D 1968 Mechanisms for metal-nonmetal transitions in transition-metal oxides and sulfides *Rev. Mod. Phys.* **40** 714
- [2] Toriyama T *et al* 2011 Peierls mechanism of the metal-insulator transition in ferromagnetic hollandite  $\text{K}_2\text{Cr}_8\text{O}_{16}$  *Phys. Rev. Lett.* **107** 266402
- [3] Nocerino E 2022 Unconventional superconductivity in the spinel thin film  $\text{LiTi}_2\text{O}_4$  investigated by low-energy SR (From Doctoral Dissertation, Kungliga Tekniska högskolan) (available at: <https://urn.kb.se/resolve?urn=urn:nbn:se:kth:diva-321992>)



- [4] Bednorz J G and Müller K A 1986 Possible highT<sub>c</sub> superconductivity in the Ba-La-Cu-O system *Z. Phys. B* **64** 189–93
- [5] Urushibara A, Moritomo Y, Arima T, Asamitsu A, Kido G and Tokura Y 1995 Insulator-metal transition and giant magnetoresistance in  $\text{La}_{1-x}\text{Sr}_x\text{MnO}_3$  *Phys. Rev. B* **51** 14103
- [6] Matsubara N et al 2020 Neutron powder diffraction study of  $\text{NaMn}_2\text{O}_4$  and  $\text{Li}_{0.92}\text{Mn}_2\text{O}_4$ : insights on spin-charge-orbital ordering *Phys. Rev. Res.* **2** 043143
- [7] Nozaki H, Sugiyama J, Månsson M, Harada M, Pomjakushin V, Sikolenko V, Cervellino A, Roessli B and Sakurai H 2010 Incommensurate spin-density-wave order in quasi-one-dimensional metallic antiferromagnet  $\text{NaV}_2\text{O}_4$  *Phys. Rev. B* **81** 100410
- [8] Taguchi M, Yamaoka H, Yamamoto Y, Sakurai H, Tsujii N, Sawada M, Daimon H, Shimada K and Mizuki J 2017 Unusual coexistence of negative and positive charge transfer in mixed-valence  $\text{Na}_x\text{Ca}_{1-x}\text{Cr}_2\text{O}_4$  *Phys. Rev. B* **96** 245113
- [9] Sakurai H, Kolodiazny T, Michiue Y, Takayama-Muromachi E, Tanabe Y and Kikuchi H 2012 Unconventional colossal magnetoresistance in sodium chromium oxide with a mixed-valence state *Angew. Chem., Int. Ed.* **51** 6653–6
- [10] Toriyama T, Konishi T and Ohta Y 2014 Electronic structure of calcium-ferrite-type Cr oxide  $\text{NaCr}_2\text{O}_4$  *Proc. Int. Conf. on Strongly Correlated Electron Systems (SCES2013)* p 017003
- [11] Sakurai H 2014 Magnetic and electronic properties of  $\text{Ca}_{(1-x)}\text{Na}_x\text{Cr}_2\text{O}_4$  double-exchange interactions and ligand holes *Phys. Rev. B* **89** 024416
- [12] Tokura Y 2000 *Colossal Magnetoresistive Oxides* (Boca Raton, FL: CRC Press)
- [13] Furukawa N 1995 Temperature dependence of conductivity in (La, Sr)  $\text{MnO}_3$  *J. Phys. Soc. Japan* **64** 3164–7
- [14] Takeda H, Shimizu Y, Itoh M, Sakurai H and Takayama-Muromachi E 2013 Magnetic frustration effects in the new colossal magnetoresistance oxide  $\text{NaCr}_2\text{O}_4$  *J. Korean Phys. Soc.* **62** 1914–8
- [15] Damay F, Martin C, Hardy V, Maignan A, André G, Knight K, Giblin S R and Chapon L C 2010 Zigzag ladders with staggered magnetic chirality in the  $s = 3/2$  compound  $\beta\text{-CaCr}_2\text{O}_4$  *Phys. Rev. B* **81** 214405
- [16] Sakurai H 2013 Novel colossal magnetoresistance in  $\text{NaCr}_2\text{O}_4$  *J. Korean Phys. Soc.* **63** 583–6
- [17] Zhang F and Rice T 1988 Effective hamiltonian for the superconducting Cu oxides *Phys. Rev. B* **37** 3759
- [18] Nozaki H et al 2018 Magnetic structure for  $\text{NaCr}_2\text{O}_4$  analyzed by neutron diffraction and muon spin-rotation *Physica B* **551** 137–41
- [19] Nozaki H, Sakurai H, Harada M, Higuchi Y, Brewer J, Ansaldò E and Sugiyama J 2014 Internal magnetic field in the zigzag-chain family (Na, Ca)  $\text{Cr}_2\text{O}_4$  *J. Phys.: Conf. Ser.* **551** 012013
- [20] Sugiyama J, Nozaki H, Harada M, Higuchi Y, Sakurai H, Ansaldò E J, Brewer J H, Keller L, Pomjakushin V and Månsson M 2015 Magnetic ground state of novel zigzag chain compounds,  $\text{NaCr}_2\text{O}_4$  and  $\text{Ca}_{1-x}\text{Na}_x\text{Cr}_2\text{O}_4$ , determined with muons and neutrons *Phys. Proc.* **75** 868–75
- [21] Nocerino E et al Na-ion dynamics in the solid solution  $\text{Na}_{1-x}\text{Ca}_x\text{Cr}_2\text{O}_4$  studied by muon spin rotation and neutron diffraction (arXiv:2211.13164)
- [22] Yamaoka H et al 2020 Electronic and crystal structures of  $(\text{Na}_{1-x}\text{Ca}_x)\text{Cr}_2\text{O}_4$  with anomalous colossal magnetoresistance *Phys. Rev. B* **102** 235150
- [23] Online resource (available at: <http://www.psi.ch/smus/InstrumentDollyEN>)
- [24] Online resource (available at: [www.psi.ch](http://www.psi.ch))
- [25] Ishigaki T et al 2009 IBARAKI materials design diffractometer (iMATERIA)-versatile neutron diffractometer at J-PARC *Nucl. Instrum. Methods Phys. Res. B* **600** 189–91
- [26] Yonemura M et al 2014 Development of SPICA, new dedicated neutron powder diffractometer for battery studies *J. Phys.: Conf. Ser.* **502** 012053
- [27] Rodríguez-Carvajal J 1993 Recent advances in magnetic structure determination by neutron powder diffraction *Physica B* **192** 55–69
- [28] Momma K and Izumi F 2008 VESTA: a three-dimensional visualization system for electronic and structural analysis *J. Appl. Crystallogr.* **41** 653–8
- [29] WaveMetrics 2017 IGOR pro, scientific data analysis software (available at: <http://www.wavemetrics.com/products/igorpro/igorpro.htm>)
- [30] Suter A and Wojek B M 2012 Musfit: a free platform-independent framework for  $\mu\text{SR}$  data analysis *Phys. Proc.* **30** 69
- [31] Blundell S 1999 Spin-polarized muons in condensed matter physics *Contemp. Phys.* **40** 175–92
- [32] Kubo R and Toyabe T 1967 A stochastic model for low field resonance and relaxation *Magn. Reson. Imaging, Proc. of XIVth Colloque Ampre* 810–23
- [33] Hayano R, Uemura Y, Imazato J, Nishida N, Yamazaki T and Kubo R 1979 Zero- and low-field spin relaxation studied by positive muons *Phys. Rev. B* **20** 850
- [34] Sugiyama J et al 2021 Pressure dependence of ferromagnetic phase boundary in  $\text{BaV}_2\text{O}_7$  studied with high-pressure  $\mu\text{SR}$  *Phys. Rev. B* **103** 104418
- [35] Nocerino E et al 2023 Magnetic nature of wolframite  $\text{MgFeO}_4$  *J. Phys.: Conf. Ser.* **2462** 012037
- [36] Datta S 1934 XLIX. Studies in paramagnetism.—I. on the mechanism of quenching of orbital magnetic moment in paramagnetic ions of the iron group *London, Edinburgh Dublin Phil. Mag. J. Sci.* **17** 585–602
- [37] Forslund O K, Ge Y, Ohta H, Wang C, Abdel-Hafiez M, Sugiyama J, Månsson M and Sassa Y Refined magnetic structure of  $\text{VI}_3$  (arXiv:2210.17455)
- [38] De Vita A et al 2022 Influence of orbital character on the ground state electronic properties in the van der Waals transition metal iodides  $\text{VI}_3$  and  $\text{CrI}_3$  *Nano Lett.* **22** 7034–41
- [39] Bhoje P A et al 2015 Electronic structure evolution across the Peierls metal-insulator transition in a correlated ferromagnet *Phys. Rev. X* **5** 041004
- [40] Yaouanc A and De Reotier P D 2011 *Muon Spin Rotation, Relaxation and Resonance: Applications to Condensed Matter* vol 147 (Oxford: Oxford University Press)
- [41] Huang K 2008 *Statistical Mechanics* (New York: Wiley)
- [42] Griffiths R B 1970 Thermodynamics near the two-fluid critical mixing point in  $\text{He}^3\text{-He}^4$  *Phys. Rev. Lett.* **24** 715
- [43] Strykowski E and Giordano N 1977 Metamagnetism *Adv. Phys.* **26** 487–650
- [44] Swüste C, Botterman A, Millenaar J and De Jonge W 1977 The magnetic phase diagram and exchange parameters in  $\text{NiCl}_2 \cdot 2\text{H}_2\text{O}$  *J. Chem. Phys.* **66** 5021–30
- [45] Schmidt V and Friedberg S 1970 Metamagnetism of  $\text{Ni}(\text{NO}_3)_2 \cdot 2\text{H}_2\text{O}$  *Phys. Rev. B* **1** 2250
- [46] Polgar L and Friedberg S 1971 Low-temperature heat capacity of the metamagnet  $\text{N}(\text{NO}_3)_2 \cdot 2\text{H}_2\text{O}$  *Phys. Rev. B* **4** 3110

- [47] Korotin M, Anisimov V, Khomskii D and Sawatzky G 1998 CrO<sub>2</sub>: a self-doped double exchange ferromagnet *Phys. Rev. Lett.* **80** 4305
- [48] Forslund O K *et al* 2021 Neutron scattering on a ferromagnetic metal-insulator transition compound K<sub>2</sub>Cr<sub>8</sub>O<sub>16</sub> (Unpublished)
- [49] Schlottmann P 2003 Double-exchange mechanism for CrO<sub>2</sub> *Phys. Rev. B* **67** 174419
- [50] Kanamori J 1959 Superexchange interaction and symmetry properties of electron orbitals *J. Phys. Chem. Solids* **10** 87–98
- [51] Dzyaloshinsky I 1958 A thermodynamic theory of “weak” ferromagnetism of antiferromagnetics *J. phys. chem. solids* **4** 241–55
- [52] Moriya T 1960 Anisotropic superexchange interaction and weak ferromagnetism *Phys. Rev.* **120** 91
- [53] Li H-F *et al* 2015 Distinct itinerant spin-density waves and local-moment antiferromagnetism in an intermetallic erpd<sub>2</sub>si<sub>2</sub> single crystal *Sci. Rep.* **5** 1–7